Realizing small-flake graphene oxide membranes for ultrafast size-dependent organic solvent nanofiltration

Nie, Lina; Goh, Kunli; Wang, Yu; Lee, Jaewoo; Huang, Yinjuan; Karahan, Huseyin Enis; Zhou, Kun; Guiver, Michael D.; Bae, Tae-Hyun

2020

Nie, L., Goh, K., Wang, Y., Lee, J., Huang, Y., Karahan, H. E., . . . Bae, T.-H. (2020). Realizing small-flake graphene oxide membranes for ultrafast size-dependent organic solvent nanofiltration. Science Advances, 6(17), eaaz9184-. doi:10.1126/sciadv.aaz9184

https://hdl.handle.net/10356/145404

https://doi.org/10.1126/sciadv.aaz9184

MATERIALS SCIENCE

Realizing small-flake graphene oxide membranes for ultrafast size-dependent organic solvent nanofiltration

Lina Nie[1]*, Kunli Goh[1,2]*, Yu Wang[3]*, Jaewoo Lee[2], Yinjuan Huang[4], H. Enis Karahan[1,2], Kun Zhou[3], Michael D. Guiver[5,6]†, Tae-Hyun Bae[1,7]†

Membranes for organic solvent nanofiltration (OSN) or solvent-resistant nanofiltration (SRNF) offer unprecedented opportunities for highly efficient and cost-competitive solvent recovery in the pharmaceutical industry. Here, we describe small-flake graphene oxide (SFGO) membranes for high-performance OSN applications. Our strategy exploits lateral dimension control to engineer shorter and less tortuous transport pathways for solvent molecules. By using La^{3+} as a cross-linker and spacer for intercalation, the SFGO membrane selective layer was stabilized, and size-dependent ultrafast selective molecular transport was achieved. The methanol permeance was up to 2.9-fold higher than its large-flake GO (LFGO) counterpart, with high selectivity toward three organic dyes. More importantly, the SFGO-La^{3+} membrane demonstrated robust stability for at least 24 hours under hydrodynamic stresses that are representative of realistic OSN operating conditions. These desirable attributes stem from the La^{3+} cross-linking, which forms uniquely strong coordination bonds with oxygen-containing functional groups of SFGO. Other cations were found to be ineffective.

INTRODUCTION

One of the most pervasive challenges faced by the pharmaceutical industry is organic solvent waste (*1*). Organic solvents currently constitute ~80% of the waste generated in a typical pharmaceutical process and ~56% of the material requirements in the production of active pharmaceutical ingredients (*1*, *2*). The high volume of waste solvents necessitates their separation and recovery, which can amount to as much as 40 to 80% of the capital and operational costs combined (*3*, *4*). Hence, the pharmaceutical industry needs to adopt more efficient technologies to meet the energy and economic demands of separating and recovering waste organic solvents. Membrane-based technology offers several competitive advantages when compared with conventional separation processes, which include energy efficiency, cost-effectiveness, robust process design, and small plant footprint (*5*). To achieve these advantages, developing high-performance organic solvent nanofiltration (OSN) membranes is deemed a strategic area of focus. Recently, membrane-selective skin layers enabled by two-dimensional graphene-based materials appear promising, as single-layer graphene has the lowest possible transport resistance, given its monoatomic thickness (*6*, *7*). In addition, graphene oxide (GO) nanosheets are highly solution processable, allowing them to be readily fabricated into laminated membranes with low-friction surface networks. This architecture facilitates ultrafast transport of water molecules within the tunable interlayer spacing, which acts as well-defined nanochannels, thus achieving precise molecular sieving (*8*, *9*). Also, the tunable physicochemical properties of GO endow the GO-based membranes with great versatility for a myriad of different membrane applications (*10*–*12*).

Compared with more established liquid-phase membrane processes such as reverse osmosis, OSN is a relatively newer technology, which is often known as solvent-resistant nanofiltration (SRNF) (*13*–*17*). The solutes to be separated typically have a molecular weight (MW) between 200 and 2000 Da (*3*). Commonly, a narrower range between 200 and 1000 Da is also reported (*13*). From the membrane stability perspective, GO-based membranes have greater relevance for OSN than for water purification. This is because they are hydrophilic, making them highly susceptible to swelling and subsequent membrane disintegration in the presence of water (*18*). GO membranes exhibit stronger membrane stability in many organic solvents (*19*). The organic solvent permeance may not always show a notable advantage over current solvent-resistant polymeric membranes (*20*). To obtain higher permeance, Huang *et al.* (*21*) synthesized solvated reduced GO (S-rGO) and demonstrated an 18-nm-thick laminated membrane with a methanol permeance close to 80 liters m^{-2} $hour^{-1}$ bar^{-1}. Recently, Yang *et al.* (*22*) also fabricated an ultrathin (8 nm) selective layer membrane based on large-flake GO (LFGO) of lateral dimensions 10 to 20 μm. Although the membrane comprised highly laminated GO with precise molecular sieving properties, the methanol permeance was low, at only ~10 liters m^{-2} $hour^{-1}$ bar^{-1}. Thus, we prepared a thicker selective layer (~70 nm) to enhance membrane stability, but incorporated two additional design strategies to maximize the separation capacity of our GO-based membranes: (i) lateral dimension control of GO nanosheets and (ii) cationic cross-linking and intercalation. The separation mechanism behind GO membranes is governed primarily by the length or tortuosity of the transport pathways and the interlayer spacing between the nanosheets (*8*, *22*, *23*). Our motivation is to demonstrate high-performance

[1]School of Chemical and Biomedical Engineering, Nanyang Technological University, Singapore 637459, Singapore. [2]Singapore Membrane Technology Centre, Nanyang Environment and Water Research Institute, Nanyang Technological University, Singapore 637141, Singapore. [3]Environmental Process Modelling Centre, Nanyang Environment and Water Research Institute, Nanyang Technological University, Singapore 637141, Singapore. [4]School of Materials Science and Engineering, Nanyang Technological University, Singapore 639798, Singapore. [5]State Key Laboratory of Engines, School of Mechanical Engineering, Tianjin University, Tianjin 300072, China. [6]Collaborative Innovation Center of Chemical Science and Engineering (Tianjin), Tianjin 300072, China. [7]Department of Chemical and Biomedical Engineering, Korea Advanced Institute of Science and Technology (KAIST), Daejeon 305-338, Republic of Korea.
*These authors contributed equally to this work.
†Corresponding author. Email: michael.guiver@outlook.com (M.D.G.); thbae@kaist.ac.kr (T.-H.B.)

ultrafast OSN by tuning the GO interlayer spacing of the membrane to engineer shorter, less tortuous pathways via controlling the lateral dimensions of the GO nanosheets (Fig. 1A).

Here, two types of GO nanosheets, small-flake GO (SFGO) and LFGO, were used for membrane fabrication via pressure-assisted filtration method. To enhance the membrane processability of SFGO, we specifically designed an ultrathin SFGO membrane cross-linked by trivalent lanthanum (III) ions to realize a chemically stable SFGO membrane (SFGO-La^{3+}). La^{3+} is chosen for its exceptional cross-linking (coordination) ability (*24*). The large ionic radius of La^{3+} makes it a suitable spacer for tuning the interlayer spacing of GO membranes (*24*). Both the SFGO-La^{3+} and La^{3+}–cross-linked LFGO (LFGO-La^{3+}) membranes were evaluated for their permeance using up to nine different types of solvents. More importantly, the separation performance of the membranes was carried out using five different organic dyes dissolved in water, methanol, and other harsher organic solvents. The long-term stability of the membranes was evaluated under two different hydrodynamic stresses driven by dead-end and cross-flow filtration, with simulation results corroborating the effectiveness of cross-linking by La^{3+} cations, and the formation of a thermodynamically favorable networks of SFGO nanosheets. These stable networks cannot be readily realized by other cations such as Co^{2+}.

RESULTS

Synthesis of ultrathin SFGO-La^{3+} and LFGO-La^{3+} membranes

The GO nanosheets used in this study were prepared via a modified Hummers' method (*25*). To achieve lateral dimension control, the GO nanosheets were subjected to specified durations of ultrasonication treatment, followed by centrifugation at different speeds (see Materials and Methods). The resulting exfoliated single-layer SFGO

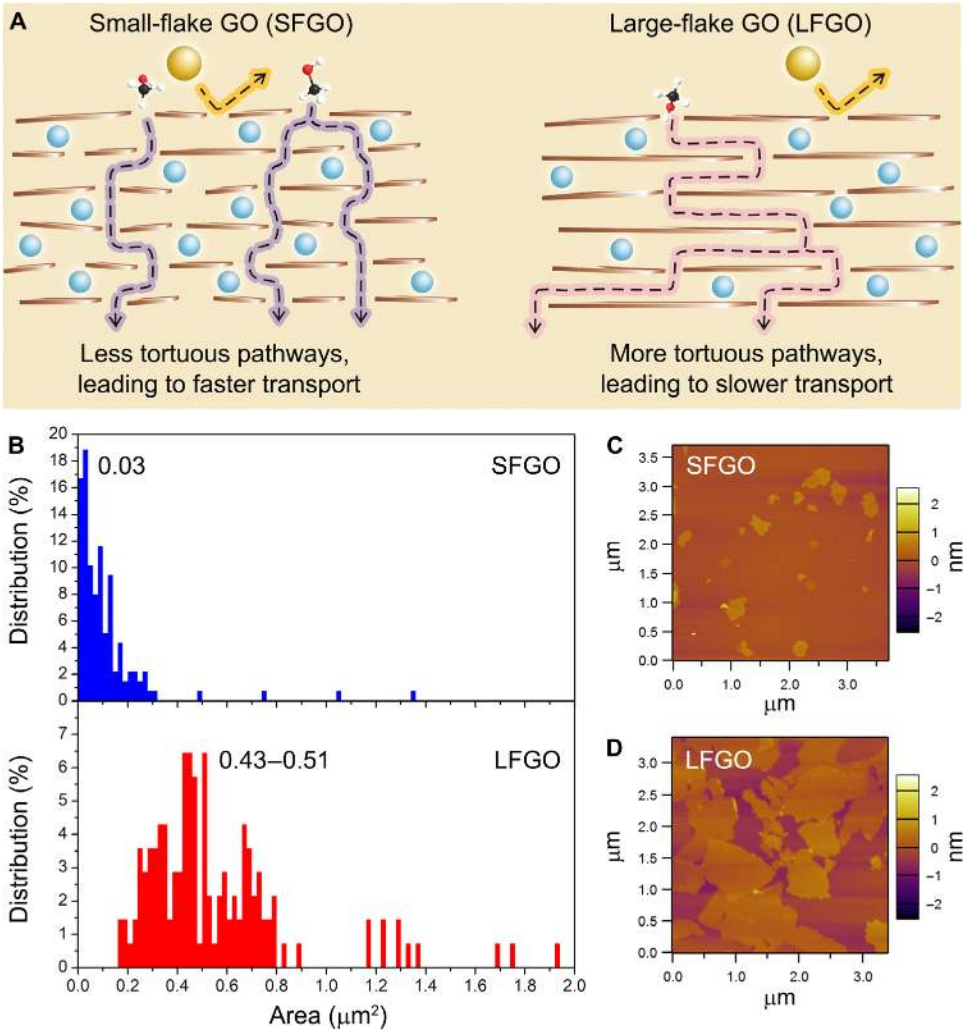

Fig. 1. Size-dependence of GO-based laminates controlled by the lateral dimension of GO nanosheets. (**A**) Schematic illustration showing the key strategy used in this work. The La^{3+} cations (blue spheres) intercalated between the GO nanosheets allow permeation of methanol (C, black; H, white; O, red) but exclude solute molecules (yellow sphere). The methanol molecule follows a less tortuous and shorter pathway (purple) for the SFGO case, leading to faster transport through the GO membrane. Using LFGO presents a more tortuous and longer pathway (red), resulting in lower methanol permeance. (**B**) The lateral dimension distribution profiles of SFGO and LFGO as denoted by their surface areas. The profiles were compiled from over 500 different AFM images. (**C** and **D**) AFM topographies showing the height images of the SFGO and LFGO nanosheets used in this work.

and LFGO (fig. S1, A and B) exhibited a several-fold difference in lateral dimensions. Accordingly, SFGO presented a mode area of 0.03 μm^2 with a narrow size distribution, while LFGO had a relatively wider distribution with a mode area in the range of 0.43 to 0.51 μm^2 (Fig. 1, B to D). The most immediate impact brought about by the large difference in lateral dimensions is apparent in the fabrication of the ultrathin membranes. A nylon substrate of pore size of 0.2 μm was chosen as the membrane support, owing to its solvent resistance, wide commercial accessibility and small pore size commonly available in the market. The pristine LFGO selective skin layer was easily assembled over the nylon substrate. Field emission scanning electron microscopic (FESEM) images show that LFGO formed a uniform and homogeneous laminate over the substrate (Fig. 2A). However, laying down a homogeneous laminate was less readily achieved for the SFGO, given that its lateral dimension was mostly smaller than the pore size of the substrate (Fig. 1B). Only a small portion of SFGO with lateral dimensions larger than the pores was successfully retained on the substrate in localized regions, but these regions were insufficient to allow propagation into a full homogeneous laminate (Fig. 2B).

Thus, to fabricate membranes with robust SFGO selective layers, we used La^{3+} cationic cross-linking to stabilize the SFGO nanosheets, with the rationale of obtaining a network of cross-linked SFGO that is sufficiently large to form a continuous laminate on the substrate. Using the same loading of 14.4 μg cm^{-2} as a comparative pristine LFGO membrane, a continuous and homogeneous laminate of SFGO-La^{3+} was successfully deposited onto the nylon substrate via pressure-assisted filtration (Fig. 2C). Visually, the ensuing SFGO-La^{3+} membrane exhibits a homogeneous surface with a smooth finish, and its mechanical flexibility suggests a high potential for robust membrane handling (Fig. 2, D and E). At the microstructure level, FESEM images also reveal a continuous surface morphology that is similar to the pristine LFGO membrane (Fig. 2, A and C). In addition, the cross-sectional morphology of the SFGO-La^{3+} membrane shows a uniform thickness of ~70 nm, which is comparable to that of the LFGO-La^{3+} membrane (Fig. 2, F and G), and the height profile that was measured using atomic force microscopy (AFM; Fig. 1C). Energy-dispersive x-ray (EDX) analysis further affirms that the La^{3+} cations are homogeneously dispersed within the SFGO-La^{3+} membrane (Fig. 2, H and I). Accordingly, on the basis of this accumulated information, the diffusion pathway of the SFGO-La^{3+} membrane is calculated to be >4.2-fold shorter than that of the LFGO-La^{3+} membrane, indicating the success of our strategy in using GO lateral dimension control to engineer a shorter transport pathway for fast solvent permeation (note S1). Intrinsic defects in GO nanosheets are common, which can also have an impact on the permeance of the GO membrane, given the potential for trans-sheet flow through pinhole defects (*26*, *27*). This result was observed by Saraswat *et al.* using GO nanosheets with two orders of magnitude difference in lateral dimension (*26*). However, the difference in lateral dimension between SFGO and LGFO is only <4-fold, and thus, we believe that

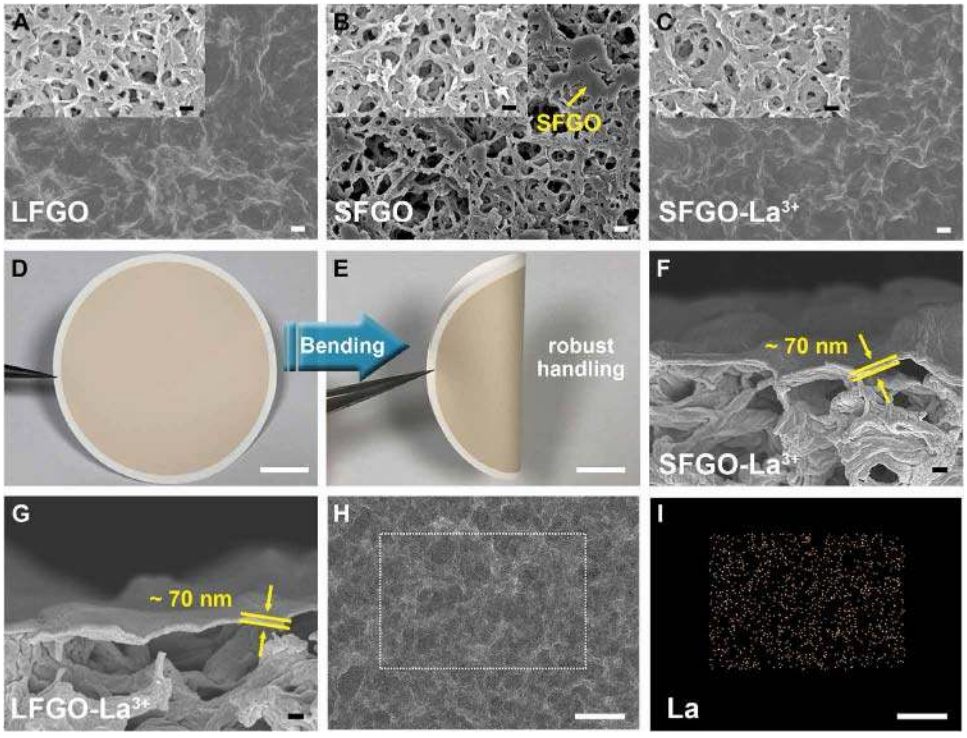

Fig. 2. Membrane characterization. (**A** to **C**) FESEM images comparing the upper surface morphologies of the pristine LFGO and SFGO membranes with that of the SFGO-La^{3+} membrane (white scale bars, 1 μm). Insets: FESEM images of the underlying nylon substrates (black scale bars, 1 μm). The incomplete laminate formation of the SFGO membrane as shown in (B) is evidenced by the similar morphologies of the surface and substrate. Only small portions of the substrate are covered by SFGO, as indicated by the yellow arrow. (**D** and **E**) Optical images of the SFGO-La^{3+} membrane, demonstrating membrane bending potentially allows robust handling. Scale bars, 1 cm. Photo credit: Lina Nie, NTU, Singapore. (**F** and **G**) FESEM images comparing cross-sectional morphologies of the SFGO-La^{3+} and LFGO-La^{3+} membranes, respectively. The thickness of the SFGO-La^{3+} and LFGO-La^{3+} laminates is geometrically estimated to be ~70 nm, as indicated by the yellow arrows and lines. Scale bars, 200 nm. (**H** and **I**) EDX element mapping of lanthanum at the upper surface of the SFGO-La^{3+} membrane, showing clearly a homogeneous distribution of the intercalated La^{3+} cations. Scale bars, 10 μm.

the impact brought by intrinsic defects is less substantial as compared with that of lateral dimension.

Next, to attest to the coordination strength of La^{3+}, we compare it with previously studied divalent cobalt (II) ion, Co^{2+}, that has been deemed promising for the control of interlayer spacing of GO (*23*, *28*). Both SFGO and LFGO aggregated almost immediately when La^{3+} cations were added to the suspensions (fig. S2, A and B). However, no aggregation occurred with Co^{2+}, as demonstrated by the clear SFGO- and LFGO-Co^{2+} suspensions upon Co^{2+} addition (fig. S2, C and D). We attribute this to the strong coordination ability of La^{3+} cations, which facilitates rapid cross-linking of SFGO to form SFGO-La^{3+} networks that are sufficiently large to appear visible. To avoid defects arising from these large networks, we performed additional ultrasonication to obtain a clear dispersion of smaller SFGO-La^{3+} networks for membrane fabrication. By carefully controlling the duration of sonication (see Materials and Methods), the smaller SFGO-La^{3+} networks maintained a stable dispersion without notable aggregation for up to 1 hour (fig. S2, E and F). At the same time, the SFGO-La^{3+} networks were sufficiently large to allow membrane processing by homogeneous deposition on the nylon substrate, before gradually showing signs of reaggregation. Compared with La^{3+} cationic cross-linking, SFGO-Co^{2+} dispersion appeared to be stable for >5 hours (fig. S2, G and H). Owing to the weaker coordination ability of Co^{2+} (*29*), SFGO-Co^{2+} was, however, unable to create large-enough networks to form a continuous laminate on the nylon substrate (fig. S3).

OSN performance

The OSN separation performance of the SFGO-La^{3+} membrane was evaluated by dead-end filtration at 1-bar pressure due to the ease and simplicity of the method. We first evaluated the permeance of water and various common organic solvents (Fig. 3A). Generally, the permeance of SFGO-La^{3+} membrane showed a predominant dependence on the viscosity of the solvent. The dependence was exemplified by the Hagen-Poiseuille equation (note S2), which showed a near inverse proportionate decrease in the permeance as the viscosity increased (fig. S4 and table S1). This result is in accordance with those from previous reports (*21*, *30*). In addition, the molecular dimension of the solvents was found to exert a considerable impact. For example, despite their similar viscosities, acetonitrile exhibited higher permeance over acetone, given its smaller molecular dimension (table S1). These results suggest that our SFGO-La^{3+} has membrane integrity equivalent to that of a continuous nanofilm (*30*). Next, we evaluated the permeance of the LFGO-La^{3+} membrane. The permeance of the LFGO-La^{3+} membrane demonstrated a similar trend with each evaluated solvent showing lower permeance than its SFGO-La^{3+} counterpart (Fig. 3A). Of particular interest is the significantly lower permeance of the LFGO-La^{3+} membrane toward acetone, acetonitrile, and methanol, which is believed to be due to the high polarity and low viscosity of the solvents, as shown in table S1 (*22*, *31*). Henceforth, in this study, we selected methanol as a model organic solvent since it has widespread use in the pharmaceutical industry (*32*, *33*). Moreover, methanol can dissolve many organic dyes, allowing subsequent membrane selectivity evaluations.

The success of our strategy is clearly reflected in the ultrafast pure methanol permeance of our GO membranes. The SFGO-La^{3+} membrane presented up to 2.7-fold higher pure methanol permeance than the LFGO-La^{3+} membrane (Fig. 3B). In addition, an order-of-magnitude-higher permeance was observed for the SFGO-La^{3+} membrane as compared with the LFGO-Co^{2+} and pristine LFGO membranes. This overall trend was similarly observed using water as the solvent, but to a different extent of increase in the permeance, owing to the higher viscosity of water (Fig. 3B). We attribute the higher methanol permeance of the SFGO-La^{3+} membrane to the shorter and less tortuous transport pathways formed by SFGO, with the less viscous methanol showing faster transport in the enlarged interlayer spacing of the La^{3+}–cross-linked GO membranes (Fig. 1A). To verify our claim, we further evaluated the membrane selectivity to provide evidence that the ultrafast methanol permeance was not the result of membrane defects. Five organic dyes of different charges and MWs—including methyl orange (MO; 327.33 g mol^{-1}), crystal violet (CV; 407.98 g mol^{-1}), acid fuchsin (AF; 585.53 g mol^{-1}), acid red 94 (AR; 1017.63 g mol^{-1}), and alcian blue (AB; 1298.86 g mol^{-1})—were dissolved in methanol and water for selectivity measurements (see table S2 for details of organic dyes). When water was used as the solvent, the SFGO-La^{3+} and LFGO-La^{3+} membranes demonstrated water permeance of ~30 and 24 liters m^{-2} $hour^{-1}$ bar^{-1}, respectively, which was accompanied by rejection rates of above 95% (Fig. 3, C and D). These results are in good agreement with those in the literature (*10*, *34*), suggesting that the quality and integrity of our membranes are comparable to current state-of-the-art graphene-based nanofiltration (NF) membranes.

More importantly, when methanol was used as the solvent for OSN application, our SFGO-La^{3+} membrane showed excellent rejection rates of above 95% for dyes with larger MWs, such as AF and AR. In particular, AB gave a rejection of almost 100% (Fig. 3E). However, because of their lower MWs, MO and CV saw a significantly lower rejection rate of 43 and 9%, respectively (Fig. 3E). The rejection rate of the negatively charged MO was noticeably higher, despite having a lower MW of 327 g mol^{-1} as compared with that of the positively charged CV at 408 g mol^{-1} (table S2). This is likely the result of electrostatic repulsion between the negatively charged solutes and the membrane surface, considering that the SFGO-La^{3+} membrane also exhibited a negative charge across a wide pH range of 3 to 9 (fig. S5). Thus, the SFGO-La^{3+} membrane appears to exclude negatively charged dye via Donnan exclusion below a MW of 586 g mol^{-1}. Above this MW cutoff, the molecular sieving effect becomes more dominant compared with Donnan exclusion, as exemplified by the high rejection rates of AF, AR, and AB, irrespective of their electrical charges. Similarly, the molecular sieving effect was also evident from the rejection results of the LFGO-La^{3+} membrane, showing rates well above 97% for the larger dyes AF, AR, and AB (Fig. 3F).

A noteworthy point is the lower solvent permeance of the SFGO-La^{3+} membrane when feeding dye solutions (Fig. 3E) as compared with pure solvents (Fig. 3, A and B). Generally, dye solutions have a lower than expected permeance due to concentration polarization (CP), which is a common phenomenon, whereby solutes accumulate at the membrane surface, resulting in a drop in the driving force (*10*, *35*). In this study, CP caused an ~12% drop in the methanol permeance of the SFGO-La^{3+} membrane, reaching an average value of ~100 liters m^{-2} $hour^{-1}$ bar^{-1} when evaluating various dye solutions (Fig. 3E). Despite this, the methanol permeance (from dye solutions) of the SFGO-La^{3+} membrane (Fig. 3E) remained 2.6-fold higher than the pure methanol permeance of the LFGO-La^{3+} membrane (Fig. 3B). Moreover, if we compare among dye solution separation performances, the SFGO-La^{3+} membrane exhibits methanol permeance of up to 2.9-fold higher than the LFGO-La^{3+} membrane at similar dye

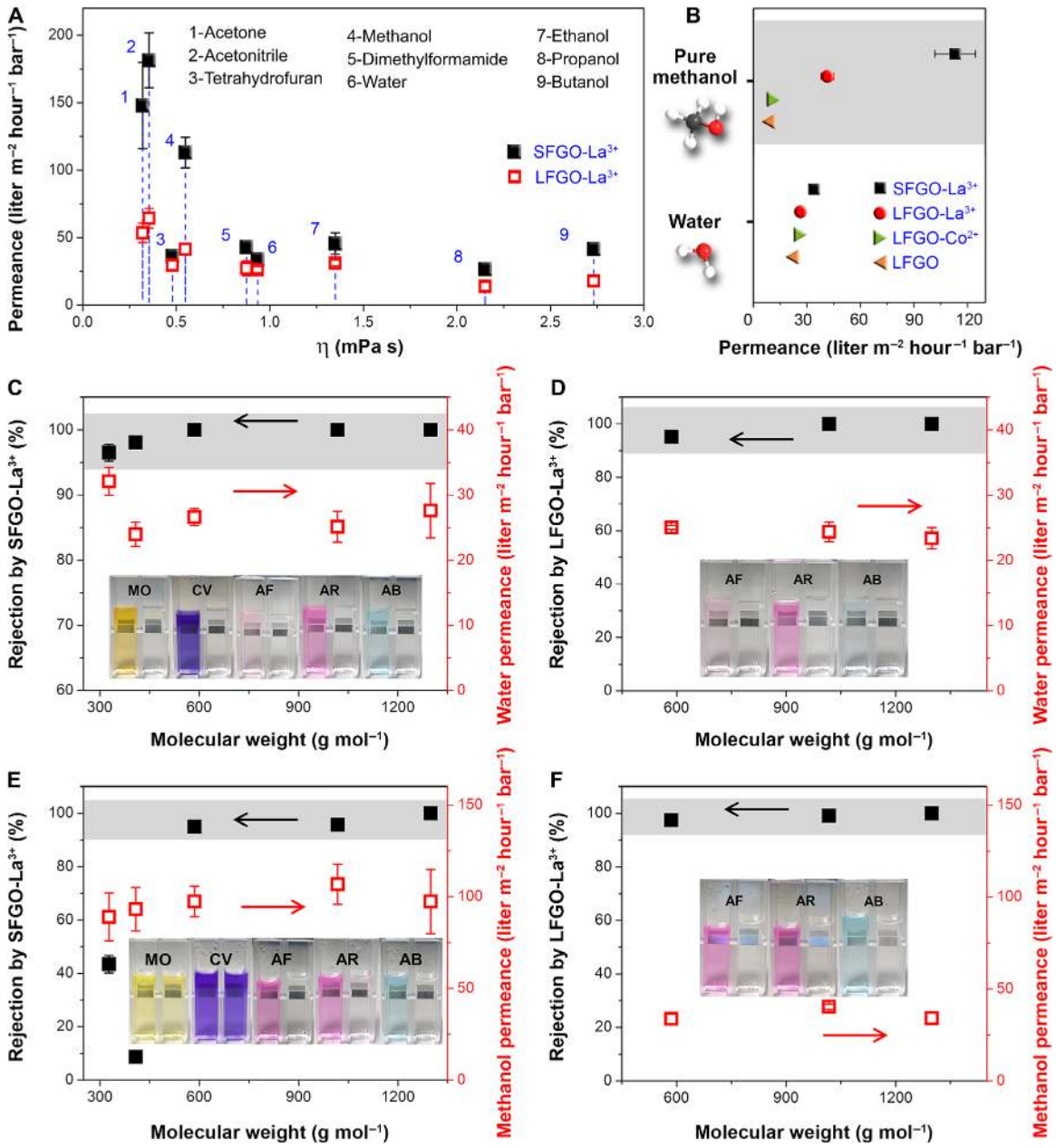

Fig. 3. OSN performances of our GO membranes. (**A**) Permeance of pure water and various pure organic solvents through the SFGO-La^{3+} and LFGO-La^{3+} membranes as a function of their viscosity. The permeance is found to be inversely proportionate to the viscosity of the solvents, indicating that the permeance through GO membranes is governed by Hagen-Poiseuille flow. (**B**) A comparison of the permeance of pure methanol and water through the pristine LFGO membrane, as well as LFGO-Co^{2+}, LFGO-La^{3+}, and SFGO-La^{3+} membranes. Notably, the SFGO-La^{3+} membrane exhibits an order-of-magnitude-higher pure methanol permeance as compared to the other membranes. (**C** to **F**) Separation performances of the SFGO-La^{3+} and LFGO-La^{3+} membranes as demonstrated by various 10-ppm solutions containing organic dyes of different charges and molecular weights in either water or methanol (see table S2 for details). The size-dependent effect is evidenced here by the higher methanol permeance of the SFGO-La^{3+} membrane than that of the LFGO-La^{3+} counterpart at high membrane selectivity. Insets: Optical images showing the colors of the dye solutions before and after the NF process. Error bars to some of the data points are not visible due to small experimental errors. Photo credit: Lina Nie, NTU, Singapore.

rejection rates (table S3). To further improve the separation performance, we performed a cross-flow filtration evaluation on the SFGO-La^{3+} membrane using AF dye solution. Because of shearing generated by the cross-flow hydrodynamics at the membrane surface, CP is alleviated, which leads to an increase in water and methanol permeances by 28 and 41%, respectively, as compared with the results obtained under dead-end filtration (table S3). The rejection rates of AF in water and methanol are also similar at almost 100 and 96%, respectively (fig. S6). These performance results not only demonstrate that our dead-end results are representative of cross-flow results at lower permeance but also support our previous hypothesis that the SFGO-La^{3+} membrane offers a shorter and less tortuous pathway for solvent

transport, and the enlarged interlayer spacing by La^{3+} intercalation further accentuates ultrafast solvent permeance, without compromising membrane selectivity.

The ultrafast solvent permeance is clearly demonstrated by a simple performance benchmarking (table S3). Our SFGO-La^{3+} membrane exhibited methanol permeance that is at least 1.3-fold higher than current state-of-the-art GO- and rGO-based membranes for OSN applications, when evaluating dye solutions (*21*, *22*, *36*, *37*). Furthermore, with up to 2.6-fold faster methanol permeance at comparable, if not better, membrane selectivity than a Mg^{2+} intercalated GO membrane (GO-Mg^{2+}) (*22*), the positive effect brought about by La^{3+} intercalation is easily distinguishable. Beyond graphene-based membranes, our SFGO-La^{3+} membrane also shows competitive OSN performance among other types of membrane designs, which include polymer nanofilms with intrinsic microporosity (*30*, *38*), nanomaterial-based (thin-film) composite membranes (*37*, *39*, *40*), and functionalized boron nitride membranes (table S3) (*41*). Together, our strategy of using SFGO with La^{3+} intercalation and cross-linking is effective in realizing continuous and robust GO-based selective layers and delivering among the best-performing solvent-resistant membranes currently reported.

Membrane characterization

To further substantiate our interpretation of the performance data, La^{3+} cross-linking of the GO selective layer was investigated in greater depth. First, Raman spectroscopy was used to validate the invariant chemical state and structural integrity of SFGO after La^{3+} cross-linking (fig. S7A). Then, x-ray diffraction (XRD) was assessed to examine the change in *d*-spacing of the SFGO-La^{3+} membrane (Fig. 4A). The *d*-spacing of pristine GO membrane in the dry state was 8.2 Å (fig. S7B), which matches previously reported values (*18*, *42*). As expected, the *d*-spacing of both SFGO-La^{3+} and LFGO-La^{3+} membranes increased to 8.8 Å with cationic intercalation (Fig. 4A and fig. S7B). The increase in *d*-spacing is not in accordance to the ionic radius of La^{3+} (~1.16 Å) (*43*) because GO nanosheets are flexible, and the interlayer spacing tends to constrict back at regions without La^{3+} intercalation, leaving only a slightly enlarged *d*-spacing (*44*). In the wet state, the SFGO-La^{3+} membrane swelled to various extents, depending on the solvents used (Fig. 4A). Notably, the *d*-spacing of the SFGO-La^{3+} membrane increased to 9.0 and 9.2 Å for membranes wetted in water and methanol, respectively. A minimal *d*-spacing enlargement of between 0.2 and 0.4 Å is typical of amine–cross-linked GO membranes, as revealed by several studies (*42*, *45*). This shows that La^{3+} cross-linking can create an effect that is comparable to the stretching resistance demonstrated by amine cross-linkers (*45*). Besides, a modulation of the *d*-spacing (within ~1.0 Å) was observed for all evaluated solvents (Fig. 4A). This increase in *d*-spacing is smaller than the size of the solvent molecules themselves, indicating that the amount of solvent intercalation never exceeds one monolayer (*46*). Hence, excessive swelling of the SFGO-La^{3+} membrane in different organic solvents is strongly mitigated by La^{3+} cross-linking (Fig. 4A). Also, because of the mitigation in swelling, our SFGO-La^{3+} membrane shows potential use with other harsher organic solvents. The permeance of dimethylformamide (DMF) and acetone were ~35 and ~126 liters m^{-2} $hour^{-1}$ bar^{-1}, respectively, with AF, AR, and AB rejection rates typically above >95%, similar to the performances in water (fig. S8). These results suggest that the enlarged *d*-spacing of the nanochannels helps to reduce the membrane resistance, which is especially evident for less viscous solvents such as acetone and methanol. The meager increase in the *d*-spacing means that the microstructure of the membrane is kept intact, giving rise to high organic dye rejections. However, as this increase is limited, we believe that the predominant reason for ultrafast solvent permeance still stems from the tuning of GO lateral dimension to obtain shorter and less tortuous transport pathways for solvent molecules.

Next, we analyzed the surface chemistry of the SFGO-La^{3+} membrane using x-ray photoelectron spectroscopy (XPS) to disclose the origin of La^{3+} cross-linking. As highlighted in Fig. 4B, the SFGO-La^{3+} membrane before performance evaluation exhibited clear La3d and La4d peaks, suggesting that the La^{3+} cations were successfully coordinated within the ultrathin GO laminate. The La/C atomic ratio is calculated at 1.7 ± 0.1%, which is comparable to that of an Al^{3+} intercalated GO membrane (*47*). The deconvolution of the $La3d_{5/2}$ peak shows peaks at binding energies of 833.2 and 836.6 eV. Significantly, the difference in the energy, ΔE, of magnitude 3.4 eV is unique to lanthanum carbonate (Fig. 4C) (*48*, *49*), suggesting that La^{3+} possibly cross-links by cationic coordination to negatively charged carboxylate groups of GO nanosheets. To further substantiate this by Fourier-transform infrared spectroscopy (FTIR), the spectrum of SFGO-La^{3+} showed additional absorption bands between 668 and 818 cm^{-1}, which correspond to the characteristic bands of hydrated lanthanum carbonate (Fig. 4D) (*50*, *51*). In particular, the band at 668 cm^{-1} is likely due to lattice vibrations of La—O (*51*). In addition, band shifts and changes were observed after cross-linking with La^{3+}. These bands are associated with C—O (1042 cm^{-1}), C—O—H (1334 and 1451 cm^{-1}), and C═O (1730 cm^{-1}) stretching vibrations (Fig. 4D) (*52*). This observation provides clear evidence to support our claim that La^{3+} cross-linking occurs via strong cationic coordination to the oxygen-containing functional groups of the GO nanosheets. The coordination was so robust that XPS provided similar La/C atomic ratio of 1.6 ± 0.2% even after an ~24-hour cross-flow hydrodynamic evaluation (fig. S9).

Membrane stability

A pertinent issue with pristine SFGO is its potential instability compared with LFGO, as already discussed in the previous section. Here, we envision compelling stability of our SFGO-La^{3+} membrane, owing to the strong coordination by La^{3+}. To corroborate the membrane stability, OSN performance and mechanical stability were investigated. The long-term performance stability of the SFGO-La^{3+} membrane was assessed by dead-end evaluation using methanol under 3-bar applied pressure. As shown in Fig. 4E, the membrane performance sustained steady ultrafast methanol permeance of >100 liters m^{-2} $hour^{-1}$ bar^{-1} for up to 24 hours. The permeance began to decrease over time but was maintained at >86 liters m^{-2} $hour^{-1}$ bar^{-1} for the 72-hour duration of the period. We attribute the drop in permeance to the compaction of the lamellar microstructure of the SFGO-La^{3+} membrane due to the higher applied pressure, as commonly reported in the literature (*26*). Nevertheless, the AF rejection rate was constantly >95% throughout the stability evaluation test. For long-term OSN operations, this observation implies that our SFGO-La^{3+} membrane has the relevant and necessary membrane stability to perform under continuous compressive stress driven by applied pressure.

Following this, we evaluated the mechanical stability of our membrane under two distinct hydrodynamic conditions. The membrane was first submerged in both methanol and water to evaluate its

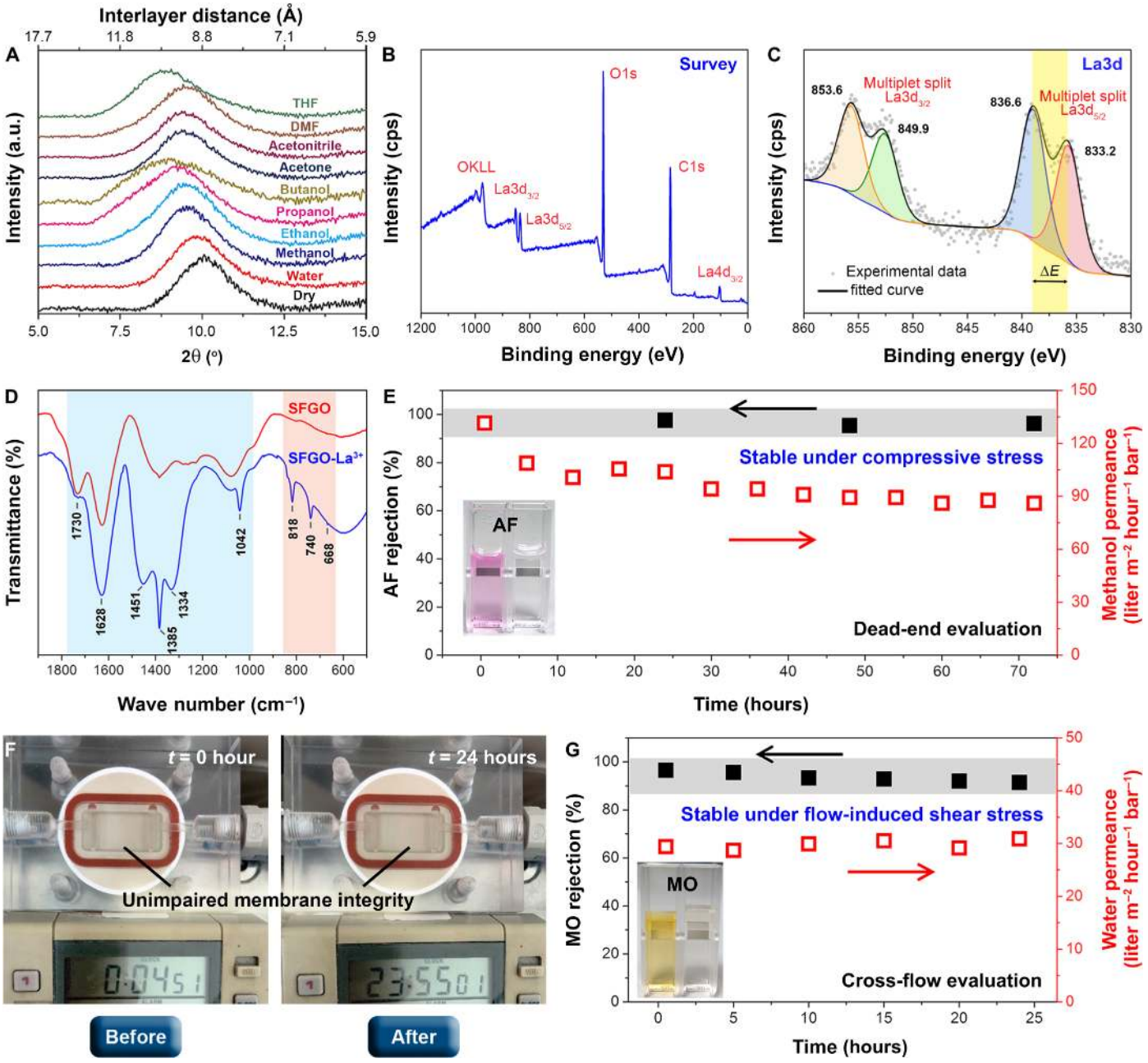

Fig. 4. Physicochemical properties and stability of the SFGO-La^{3+} membrane. (**A**) XRD patterns of the SFGO-La^{3+} membrane, showing a shift in the (002) peak and interlayer spacing between SFGO nanosheets when dried, as well as in water and a multitude of organic solvents. Despite this shift, the change in interlayer spacing (excluding intrinsic SFGO thickness) is at most ~1.0 Å, suggesting monolayer intercalation by solvent molecules and swelling mitigation by La^{3+} cross-linking. (**B** and **C**) XPS data showing the survey scan of the SFGO-La^{3+} membrane before performance evaluation and the La3d peaks with ΔE of 3.4 eV (highlighted in yellow), which is characteristic of lanthanum carbonate. (**D**) FTIR spectra with new absorption bands appearing at 668, 740, and 818 cm^{-1} (highlighted in red) of the SFGO-La^{3+} spectrum. The band at 668 cm^{-1} indicates the presence of La—O lattice vibrations. Also, band shifts and changes (highlighted in blue) confirm La^{3+} coordination to oxygen-containing functional groups of SFGO. (**E**) Membrane stability of the SFGO-La^{3+} membrane under a long-term compressive stress of 3-bar applied pressure as demonstrated by the stable methanol permeance and high AF rejection rate of >95% for up to 72 hours. Inset: Optical image showing the color of the AF solution before and after the NF process at 72 hours. Photo credit: Lina Nie, NTU, Singapore. (**F**) Membrane stability of the SFGO-La^{3+} membrane for up to 24 hours under flow-induced shear stress driven by cross-flow hydrodynamics of rate 1400 ml min^{-1}. Visual comparison of the optical images suggests that membrane integrity is unimpaired after the cross-flow evaluation. Photo credit: Lina Nie, NTU, Singapore. (**G**) The unimpaired integrity after cross-flow evaluation is also substantiated by the long-term cross-flow stability of the SFGO-La^{3+} membrane, as demonstrated by the stable water permeance and high MO rejection rate of >90% for up to 24 hours. Inset: Optical image showing the color of the MO solution before and after the NF process at 24 hours. Photo credit: Lina Nie, NTU, Singapore.

long-term swelling capacity and stability, which is a common protocol used in academic research to demonstrate the stability of GO-based membranes (*10*, *47*). Owing to the strong La^{3+} cross-linking, our SFGO-La^{3+} membrane exhibited expectedly good stability in water and methanol, with limited membrane swelling, as evidenced by its intactness after 30 days (fig. S10, A and B). However, this steady-state hydrodynamic condition is unrepresentative of practical applications. Hence, we subjected the membrane to unsteady-state cross-flow hydrodynamic stress. Previously, the SFGO-La^{3+} membrane was able to resist flow-induced shearing at a rate of 100 ml min^{-1} during the cross-flow evaluations. Here, we increased the cross-flow rate to 1400 ml min^{-1}. This rate is equivalent to a cross-flow velocity of 1.56 m s^{-1} and a Reynolds number of 3119 that is transitional between laminar and turbulent flow (note S3) (*53*). Notably, the SFGO-La^{3+} membrane withstood this high cross-flow rate for up to ~24 hours without showing any visible signs of damage (Fig. 4F). This stability was also exemplified by the stable water permeance and high MO rejection rate of >90% for up to 24 hours, indicating robust membrane integrity under high hydrodynamic shear stress (Fig. 4G). In contrast, the pristine LFGO membrane without La^{3+} cross-linking showed poor stability under cross-flow hydrodynamics. This was corroborated by a much lower MO rejection rate of 41% after the 24-hour cross-flow evaluation as compared to the >90% rejection rate exhibited by the La^{3+} cross-linked GO membranes (fig. S10C). Hence, we demonstrate that our SFGO-La^{3+} membrane has a much higher capacity to withstand persistent compressive stress and unsteady-state hydrodynamics encountered under realistic OSN operating conditions. We attribute this to La^{3+} coordination, which not only renders individual SFGO into a more extensive network of cross-linked SFGO but also controls interlayer spacing by chemically anchoring the SFGO together, making them less susceptible to flow-induced shearing at the membrane surface and creeping under hydraulic pressure.

DISCUSSION

In this study, ultrafast permeance of the SFGO membrane is realized by a size-dependent effect based on a shorter and less tortuous pathway coupled with an enlarged interlayer spacing for the fast transport of solvent molecules. Concertedly, good membrane selectivity toward organic dyes and potential long-term membrane stability under realistic hydrodynamic conditions are achieved. These desirable attributes are enabled by La^{3+} cross-linking of GO nanosheets with small lateral dimensions, which is instrumental in stabilizing the membrane to create a robust and conformal selective layer that is essential for delivering an outstanding membrane performance for OSN applications. On the basis of spectroscopic evidence, we have associated the source of La^{3+} cross-linking to the coordination bonds formed between the cations and oxygen-containing functional groups of SFGO nanosheets. Comparative metal ions, such as Co^{2+} reported previously, were found to be ineffective. To gain further insights into La^{3+} cross-linking, we also computationally explored the driving force behind the proposed coordination bonds. First, density functional theory (DFT) calculations were carried out to understand the interactions between SFGO and La^{3+} cations. We constructed a SFGO-La^{3+} system with two La^{3+} cations sandwiched between two SFGO flakes in a periodic box with explicit water molecules (see Materials and Methods; Fig. 5A). Structural optimization suggests that the hydrated La^{3+} cations coordinate to the carboxyl groups at the edge, as well as hydroxyl and epoxy groups at the upper and lower SFGO flake surfaces, forming an extensive SFGO network as previously deduced (Fig. 5A). The conclusion is further substantiated by a deformation charge density calculation, which shows that the electron-rich highest occupied molecular orbitals (HOMOs) of the oxygen-containing groups of SFGO are oriented toward the electron-deficient empty 5d orbitals of the La^{3+} cations, facilitating electron transfer between the two entities (Fig. 5B). This outcome implies that the electrons are capable of delocalizing extensively within the SFGO-La^{3+} network to bestow additional stability to the La—O coordination bonds.

To offer a more intuitive demonstration of the stability of La^{3+} cross-linking, we performed first-principles molecular dynamics (FPMD) simulation on the SFGO-La^{3+} system at 298 K. As presented in Fig. 5C, snapshots at successive time frames of 0.5, 7.5, and 15 ps show that the structural integrity and interlayer spacing of the SFGO-La^{3+} system remain almost unchanged throughout the course of the simulation, although some slight geometrical distortion in the coordination bond was observed. Notably, the total energy of the system decreases rapidly within the first 0.5 ps of La—O bond formation (Fig. 5C) and then continues to evolve into a more stable configuration, reaching a final total energy of −6.23 eV per atom at 15 ps. Such a stability is not easily replicated by exploiting metal cations other than La^{3+}. For example, we conducted the same FPMD simulation on a SFGO-Co^{2+} system (fig. S11) and observed that the upper Co^{2+} cation was not securely cross-linked to the SFGO nanosheets. Within the time frame of 15 ps, the Co^{2+} cation appeared to move away from the lower coordinated SFGO flake to the one above it and attempted to shift out of the stipulated periodic box (Fig. 5D). The dynamic state of the SFGO-Co^{2+} system suggests that the electron delocalization cannot be extended beyond discrete Co—O bonds, resulting in less stable Co—O coordination bonds as compared with the La—O counterpart. This deduction is evidenced by the higher total energy of the SFGO-Co^{2+} system at −6.16 eV per atom at 15 ps (Fig. 5D). In retrospect, the simulation results are consistent with our experimental findings and account for the observation that the less stable SFGO-Co^{2+} networks are not sufficiently large to form a continuous homogeneous selective layer.

In summary, we successfully realize a size-dependent effect using thermodynamically favorable networks of SFGO nanosheets for membrane-based OSN or SRNF applications. Strong La^{3+} intercalation and cross-linking provide robust, thin, and continuous SFGO-La^{3+} membranes with an order-of-magnitude-higher methanol permeance than pristine LFGO membrane, accompanied by high selectivity toward a number of organic dyes. We attribute the ultrafast permeance to the shorter and less tortuous transport pathway as well as the enlarged interlayer spacing of the SFGO-La^{3+} membrane. The high selectivity is a result of Donnan exclusion effect for negatively charged solutes below a MW of 586 g mol^{-1} and a combined effect of Donnan exclusion and molecular sieving for solutes above this MW. For potential realistic operations, membrane stability arising from strong La^{3+} cross-linking provides robustness and long-term membrane performance to handle unsteady-state hydrodynamics such as flow-induced shearing and compressive stress under applied hydraulic pressure. The strong La^{3+} cross-linking stems from coordination bonds formed between La^{3+} cations and oxygen-containing functional groups of SFGO nanosheets. Extensive electron delocalization within the SFGO-La^{3+} networks further reinforces the La—O bonds, imparting stability that is not easily replicated by other metal cations.

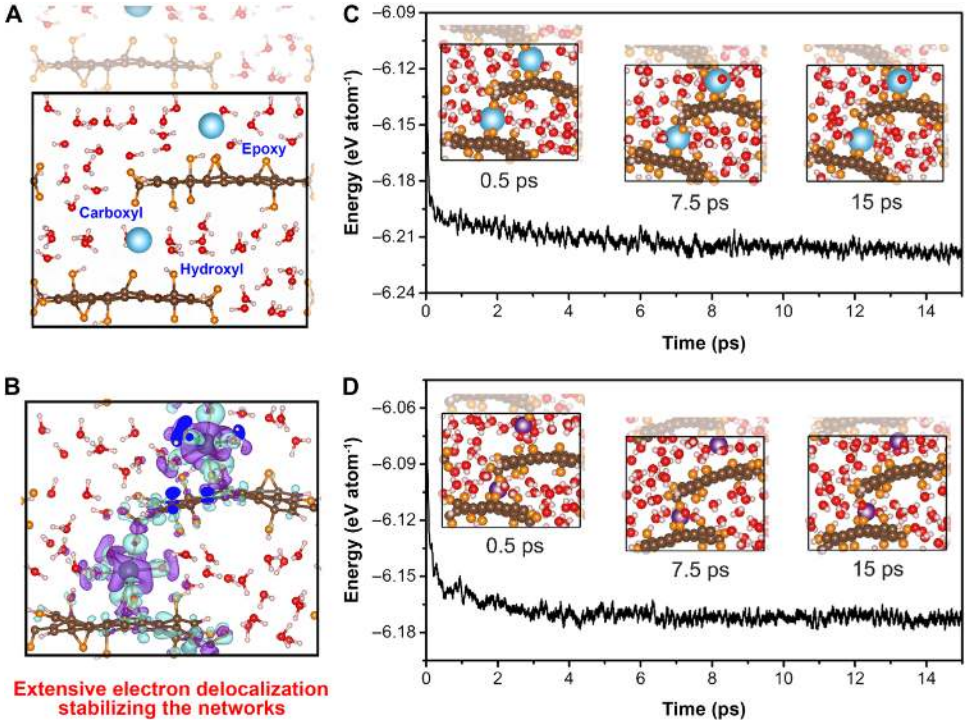

Fig. 5. Theoretical simulations of the SFGO-La^{3+} system. (**A**) An illustration of the geometrically optimized SFGO-La^{3+} model system used in the DFT simulation, where the blue, white, and red spheres represent the La^{3+} cations, as well as H and O atoms of the water molecules, respectively. The brown and orange spheres represent the C and O atoms of the SFGO nanosheets, respectively. The black solid line indicates the periodic box used in the simulation, within which two SFGO flakes interact with two La^{3+} cations via epoxy, hydroxyl, and carbonyl functional groups. (**B**) Deformation charge density of the SFGO-La^{3+} system, where the cyan and violet orbitals represent electron-rich and electron-deficient regions, respectively. On the basis that electrons move freely within the SFGO flakes, extensive electron delocalization across the SFGO-La^{3+} network can be potentially realized. (**C**) Total energy as a function of time based on FPMD simulations of the SFGO-La^{3+} at 298 K. (**D**) Comparative SFGO-Co^{2+} system at 298 K. Insets: Snapshots of the model at time frames of 0.5, 7.5, and 15 ps. The purple spheres represent the Co^{2+} cations in the SFGO-Co^{2+} system.

MATERIALS AND METHODS

GO synthesis

GO was synthesized by a modified Hummers' method (*25*). Graphite flakes (1.2 g, 99% carbon basis, and −325 mesh; Sigma-Aldrich) were dispersed in sulfuric acid (60 ml, 95.0 to 98.0%) at room temperature under magnetic stirring. Potassium permanganate (7.2 g, >99%) was added gradually to the solution over 10 min to avoid the temperature exceeding 25°C. After 15 min of stirring, nitric acid (1.3 ml, >90.0%) was added. The resulting mixture was maintained at 35°C for 2 hours using an oil bath. Following this, deionized (DI) water (120 ml) was added cautiously to the mixture very slowly, with violent effervescence ensuing upon addition. The temperature of the oil bath was then increased to 100°C and maintained at that temperature for 0.5 hour. The light-brown suspension was diluted with more DI water (300 ml) and allowed to react for an additional 0.5 hour. Then, the suspension was transferred to an ice bath. After about 0.5 hour, the mixture was treated with hydrogen peroxide (12 ml, 30%) and stirred for 0.5 hour. Last, the mixture was collected and washed several times with DI water until the pH was between 6 and 7. The final product underwent dialysis for 24 hours to remove metal ions and residual acid. The prepared GO suspension was used for membrane fabrication.

Preparation of GO membranes

All GO membranes were prepared by a pressure-assisted filtration method onto nylon substrates (47-mm-diameter Millipore filters with 0.2-μm pore size). To obtain uniform and homogeneous membranes, the stock GO suspension was diluted to a concentration of 0.01 mg ml^{-1} before membrane preparation. The cross-linking procedure was carried out by dropwise addition of 2 ml of 0.01 M $La(NO_3)_3$ or $Co(NO_3)_2$ into 200 ml of diluted GO suspension under vigorous magnetic stirring. As the La^{3+}–cross-linked GO solution started to agglomerate soon after cross-linking, the La^{3+}–cross-linked GO suspension was sonicated in an ice-water bath for 1 hour and then immediately used for membrane preparation. After sonication, the La^{3+}–cross-linked GO suspension remained stable throughout the membrane preparation process. Comparative pristine GO membranes, without the presence of metal ions, were prepared using dilute GO suspensions. All membranes were prepared using the same GO loading of 0.144 g m^{-2} and then dried in a desiccator at room temperature for 24 hours before performance evaluations or characterization.

Two types of GO nanosheets, SFGO and LFGO, were used to prepare membranes for the present study. These GO nanosheets differed in their lateral dimensions, which were controlled via ultrasound-assisted exfoliation and centrifugal separation. For the preparation of SFGO, the as-prepared GO nanosheets were sonicated (750 W) in an ice-water bath for 2 hours and subsequently centrifuged three times at 12,000 rpm for 10 min. Since the GO nanosheets with smaller lateral sizes were lighter, they remained in the supernatant while the larger flakes precipitated. Thus, the supernatant was collected and used for the preparation of SFGO membranes. For LFGO, the GO suspension was exfoliated by a 5-min ultrasonication and

then centrifuged at 3000 rpm for 10 min to separate the unexfoliated GO nanosheets. Then, the GO supernatant was further centrifuged at 12,000 rpm to separate the small GO nanosheets from the large ones. At this step, the sediment was collected and redispersed in water as LFGO for membrane fabrication.

Characterization

AFM (Asylum Research Cypher S AFM in AC mode imaging) was used to measure the lateral dimension and thickness of the prepared GO nanosheets. The lateral size distributions of the SFGO and LFGO nanosheets were obtained by analyzing over 500 samples each. FESEM (JEOL JSM-7600F) was used to image the surface morphology and thickness of the GO membranes at 5 kV. EDX spectroscopy was performed to map out the La element within the GO membranes. The concentration of the organic dyes in the feed and permeate solutions was obtained by ultraviolet-visible (UV-Vis) spectroscopy using a Shimadzu UV 2450 spectrometer with halogen lamp and deuterium lamp (200 to 900 nm). Powder X-ray diffraction (PXRD) was measured using a Bruker D2 PHASER diffractometer with Cu K_α radiation (λ = 1.5418 Å) operating at 30 kV and 10 mA. The data were collected in the 2θ range of 5° to 15°. Because of the uneven surface of the nylon substrate and the disorderliness in the membranes caused by the intercalation of La^{3+} or Co^{2+} ions, the signal intensity was very weak. Hence, the XRD results reported in this work were obtained separately from thick freestanding GO membranes. A PerkinElmer FTIR spectrophotometer was used to characterize the functional groups present in the membranes over a wavenumber range of 400 to 2000 cm^{-1}. An electrokinetic analyzer (SurPASS 3, Anton Paar, Austria) was used to quantify the surface charge of the SFGO-La^{3+} membrane by streaming potential over a pH range of 3 to 9 using an adjustable gap cell of size 20 mm × 10 mm. The structural integrity of SFGO-La^{3+} was characterized by a confocal Raman microscope XploRA PLUS (HORIBA Scientific, Japan) using a 532-nm laser. The chemical composition of the SFGO-La^{3+} membrane was quantified by XPS on Kratos AXIS Supra equipped with an automated dual anode (Al/Ag K_α) x-ray monochromatic source.

Membrane performance evaluation

The solvent permeance and rejection capacity through various GO membranes were measured using a high-pressure stirred cell (Sterlitech HP4750) at 1-bar pressure under dead-end filtration mode. For each performance evaluation, the results were an average of the data from at least three membranes with statistical errors calculated from the SDs. The permeance of water and various organic solvents was recorded only after the flux reached steady state, which was typically achieved within 0.5 hour of commencing the experiment. Permeance, P (liter m^{-2} $hour^{-1}$ bar^{-1}), was calculated by Eq. 1

$$P = \frac{V}{At\Delta p} \quad (1)$$

where V is the volume (liters) of permeate collected, A is the effective membrane area (m^2), t is the permeation time (hours), and Δp is the hydraulic pressure (bar) applied for dead-end filtration. The effective membrane area for these evaluations was 8.04 cm^2.

Five different organic dyes, namely, MO, CV, AF, AR, and AB (Sigma-Aldrich), were each dissolved in water, methanol, acetone, and DMF to afford solutions with 10-ppm concentration for membrane selectivity evaluations. The rejection rates of the organic dyes, R (%), were calculated by Eq. 2

$$R = \left(1 - \frac{C_p}{C_f}\right) \times 100\% \quad (2)$$

where C_p and C_f are the concentration of the organic dyes in the permeate and feed solution, respectively. The concentrations of the dye solutions were quantified using UV-Vis spectroscopy.

The performance of SFGO-La^{3+} membrane was also investigated under cross-flow filtration mode. A cross-flow rate of 100 ml min^{-1} was supplied using a benchtop gear pump (Fluid-o-Tech MKCS11S), and the applied pressure was maintained at 1 bar. The membrane was preconditioned by compaction for 30 min before performance evaluation using AF organic dye dissolved in either water or methanol at 10-ppm concentration.

Membrane stability evaluation

The long-term stability was examined by dead-end filtration using methanol through SFGO-La^{3+} membranes at 3-bar applied pressure for 72 hours. The mechanical stability of the SFGO-La^{3+} membrane was evaluated using two methods. First, the membrane was cut into smaller pieces of size 1 cm × 1 cm and submerged in covered petri dishes filled with water and methanol at 25°C. The integrity of the membrane pieces was visually monitored for 30 days. Second, the membrane stability was evaluated under cross-flow hydrodynamics using a method reported in our previous work (*18*). The pristine LFGO, LFGO-La^{3+}, and SFGO-La^{3+} membranes were subjected to a cross-flow rate as high as 1400 ml min^{-1} using a home-made cross-flow cell. The gear pump was used to supply DI water to the cell, and the actual flow rate was monitored by a turbine flow-meter (FTB-1301). The membranes were initially subjected to a low cross-flow rate of 100 ml min^{-1}. This was followed by a gradual increase before a final maximum flow rate of 1400 ml min^{-1} was reached and kept constant for 24 hours. The flow rate was then converted into a Reynolds number, R_e, which is a dimensionless value used to define the flow pattern imposed on the membrane surfaces (note S3). After the cross-flow tests, the membrane selectivity toward MO was re-examined to evaluate the integrity of the GO membranes. The effective membrane areas used in this case were each 3.0 cm × 1.5 cm.

Computational parameters

The fundamental mechanism of the SFGO-La^{3+} system was explored using first-principles DFT as implemented in the Vienna Ab initio Simulation Package (VASP) version 5.4.4 (*54*). The exchange-correlation energy was modeled by a Perdew-Burke-Ernzerhof (PBE) functional approach (*55*), while the ion-electron interaction was treated using a projector-augmented wave approach (*56*). A cutoff energy of 360 eV and a Monkhorst-Pack grid of 1 × 3 × 1 of k point were used in both geometrical optimizations and FPMD simulations. The higher energy cutoff and denser k point sampling were tested and found not to affect the cross-linking of the SFGO-La^{3+} system. To provide a more accurate description of the weak interactions, we applied the Grimme's D3 van der Waals corrections in all computational systems (*57*). Spin polarization and a Gaussian smearing of 0.1 eV were used, and the convergence threshold of energy was set as 5×10^{-5} eV. The NVT (N is the number of particle, V is the volume and T is temperature) ensemble was adopted in our FPMD calculations, where the time duration was set at 15 ps, with a time step of 1.0 fs. The temperature

was kept at 298 K by a Nosé-Hoover approach (*58*). It is noteworthy to mention that the MD systems were in equilibrium starting from ~7 ps.

Computational models

The SFGO-La^{3+} system was modeled with two La^{3+} cations sandwiched between two GO flakes in a periodic box. The solvent effect of water was explicitly considered by filling 46 water molecules in the box. For the construction of the GO flake, the optimal lattice parameters of pristine graphene unit cell were first identified ($a = b = 2.46$ Å), followed by addition of functional groups on the graphene supercell flake (three repeat units and armchair edge) based on a Lerf-Klinowski model (*59*). The unit cell in the x and y directions were 20.50 and 8.52 Å, respectively. The value used for the initial interlayer spacing of the SFGO-La^{3+} membrane was experimentally obtained from our XRD results at 8.8 Å (Fig. 4A). For visualization, we used the Visualization for Electronic and Structural Analysis (VESTA) code (*60*). The same computational model was also repeated for the SFGO-Co^{2+} system as a comparison.

SUPPLEMENTARY MATERIALS

Supplementary material for this article is available at http://advances.sciencemag.org/cgi/content/full/6/17/eaaz9184/DC1

REFERENCES AND NOTES

1. S. K. Ritter, Reducing environmental impact of organic synthesis. *Chem. Eng. News* **91**, 22–23 (2013).
2. R. K. Henderson, C. Jiménez-González, D. J. C. Constable, S. R. Alston, G. G. A. Inglis, G. Fisher, J. Sherwood, S. P. Binks, A. D. Curzons, Expanding GSK's solvent selection guide – embedding sustainability into solvent selection starting at medicinal chemistry. *Green Chem.* **13**, 854–862 (2011).
3. P. Marchetti, M. F. Jimenez Solomon, G. Szekely, A. G. Livingston, Molecular separation with organic solvent nanofiltration: A critical review. *Chem. Rev.* **114**, 10735–10806 (2014).
4. R. P. Lively, D. S. Sholl, From water to organics in membrane separations. *Nat. Mater.* **16**, 276–279 (2017).
5. C. Y. Chuah, K. Goh, Y. Yang, H. Gong, W. Li, H. E. Karahan, M. D. Guiver, R. Wang, T.-H. Bae, Harnessing filler materials for enhancing biogas separation membranes. *Chem. Rev.* **118**, 8655–8769 (2018).
6. K. Celebi, J. Buchheim, R. M. Wyss, A. Droudian, P. Gasser, I. Shorubalko, J.-I. Kye, C. Lee, H. G. Park, Ultimate permeation across atomically thin porous graphene. *Science* **344**, 289–292 (2014).
7. J. Zhao, G. He, S. Huang, L. F. Villalobos, M. Dakhchoune, H. Bassas, K. V. Agrawal, Etching gas-sieving nanopores in single-layer graphene with an angstrom precision for high-performance gas mixture separation. *Sci. Adv.* **5**, eaav1851 (2019).
8. H. Huang, Z. Song, N. Wei, L. Shi, Y. Mao, Y. Ying, L. Sun, Z. Xu, X. Peng, Ultrafast viscous water flow through nanostrand-channelled graphene oxide membranes. *Nat. Commun.* **4**, 2979 (2013).
9. C. Cheng, G. Jiang, C. J. Garvey, Y. Wang, G. P. Simon, J. Z. Liu, D. Li, Ion transport in complex layered graphene-based membranes with tuneable interlayer spacing. *Sci. Adv.* **2**, e1501272 (2016).
10. K. Goh, H. E. Karahan, L. Wei, T.-H. Bae, A. G. Fane, R. Wang, Y. Chen, Carbon nanomaterials for advancing separation membranes: A strategic perspective. *Carbon* **109**, 694–710 (2016).
11. G. Liu, W. Jin, N. Xu, Graphene-based membranes. *Chem. Soc. Rev.* **44**, 5016–5030 (2015).
12. K. Choi, A. Droudian, R. M. Wyss, K.-P. Schlichting, H. G. Park, Multifunctional wafer-scale graphene membranes for fast ultrafiltration and high permeation gas separation. *Sci. Adv.* **4**, eaau0476 (2018).
13. P. Vandezande, L. E. M. Gevers, I. F. J. Vankelecom, Solvent resistant nanofiltration: Separating on a molecular level. *Chem. Soc. Rev.* **37**, 365–405 (2008).
14. S. Basu, M. Maes, A. Cano-Odena, L. Alaerts, D. E. De Vos, I. F. J. Vankelecom, Solvent resistant nanofiltration (SRNF) membranes based on metal-organic frameworks. *J. Membr. Sci.* **344**, 190–198 (2009).
15. K. Vanherck, G. Koeckelberghs, I. F. J. Vankelecom, Crosslinking polyimides for membrane applications: A review. *Prog. Polym. Sci.* **38**, 874–896 (2013).
16. S. Hermans, H. Mariën, C. Van Goethem, I. F. J. Vankelecom, Recent developments in thin film (nano)composite membranes for solvent resistant nanofiltration. *Curr. Opin. Chem. Eng.* **8**, 45–54 (2015).
17. Y. Li, L. H. Wee, J. A. Martens, I. F. J. Vankelecom, Interfacial synthesis of ZIF-8 membranes with improved nanofiltration performance. *J. Membr. Sci.* **523**, 561–566 (2017).
18. K. Goh, W. Jiang, H. E. Karahan, S. Zhai, L. Wei, D. Yu, A. G. Fane, R. Wang, Y. Chen, All-carbon nanoarchitectures as high-performance separation membranes with superior stability. *Adv. Funct. Mater.* **25**, 7348–7359 (2015).
19. L. Huang, Y. Li, Q. Zhou, W. Yuan, G. Shi, Graphene oxide membranes with tunable semipermeability in organic solvents. *Adv. Mater.* **27**, 3797–3802 (2015).
20. S. K. Lim, K. Goh, T.-H. Bae, R. Wang, Polymer-based membranes for solvent-resistant nanofiltration: A review. *Chin. J. Chem. Eng.* **25**, 1653–1675 (2017).
21. L. Huang, J. Chen, T. Gao, M. Zhang, Y. Li, L. Dai, L. Qu, G. Shi, Reduced graphene oxide membranes for ultrafast organic solvent nanofiltration. *Adv. Mater.* **28**, 8669–8674 (2016).
22. Q. Yang, Y. Su, C. Chi, C. T. Cherian, K. Huang, V. G. Kravets, F. C. Wang, J. C. Zhang, A. Pratt, A. N. Grigorenko, F. Guinea, A. K. Geim, R. R. Nair, Ultrathin graphene-based membrane with precise molecular sieving and ultrafast solvent permeation. *Nat. Mater.* **16**, 1198–1202 (2017).
23. L. Chen, G. Shi, J. Shen, B. Peng, B. Zhang, Y. Wang, F. Bian, J. Wang, D. Li, Z. Qian, G. Xu, G. Liu, J. Zeng, L. Zhang, Y. Yang, G. Zhou, M. Wu, W. Jin, J. Li, H. Fang, Ion sieving in graphene oxide membranes via cationic control of interlayer spacing. *Nature* **550**, 380–383 (2017).
24. X. Li, W. Liu, Z. Guo, M. Tan, Trinuclear to dinuclear: A radii dependence lanthanide(III) self-assembly coordination behavior of an amide-type tripodal ligand. *Inorg. Chem.* **42**, 8735–8738 (2003).
25. J. Lee, H.-R. Chae, Y. J. Won, K. Lee, C.-H. Lee, H. H. Lee, I.-C. Kim, J.-m. Lee, Graphene oxide nanoplatelets composite membrane with hydrophilic and antifouling properties for wastewater treatment. *J. Membr. Sci.* **448**, 223–230 (2013).
26. V. Saraswat, R. M. Jacobberger, J. S. Ostrander, C. L. Hummell, A. J. Way, J. Wang, M. T. Zanni, M. S. Arnold, Invariance of water permeance through size-differentiated graphene oxide laminates. *ACS Nano* **12**, 7855–7865 (2018).
27. K. Erickson, R. Erni, Z. Lee, N. Alem, W. Gannett, A. Zettl, Determination of the local chemical structure of graphene oxide and reduced graphene oxide. *Adv. Mater.* **22**, 4467–4472 (2010).
28. G. Shi, J. Liu, C. Wang, B. Song, Y. Tu, J. Hu, H. Fang, Ion enrichment on the hydrophobic carbon-based surface in aqueous salt solutions due to cation-π interactions. *Sci. Rep.* **3**, 3436 (2013).
29. D. Cheng, M. A. Khan, R. P. Houser, Novel sandwich coordination polymers composed of cobalt(II), 1,2,4,5-benzenetetracarboxylato ligands, and homopiperazonium cations. *Cryst. Growth Des.* **2**, 415–420 (2002).
30. S. Karan, Z. Jiang, A. G. Livingston, Sub–10 nm polyamide nanofilms with ultrafast solvent transport for molecular separation. *Science* **348**, 1347–1351 (2015).
31. R. Liu, G. Arabale, J. Kim, K. Sun, Y. Lee, C. Ryu, C. Lee, Graphene oxide membrane for liquid phase organic molecular separation. *Carbon* **77**, 933–938 (2014).
32. D. J. C. Constable, C. Jimenez-Gonzalez, R. K. Henderson, Perspective on solvent use in the pharmaceutical industry. *Org. Process Res. Dev.* **11**, 133–137 (2007).
33. D. Prat, A. Wells, J. Hayler, H. Sneddon, C. R. McElroy, S. Abou-Shehada, P. J. Dunn, CHEM21 selection guide of classical- and less classical-solvents. *Green Chem.* **18**, 288–296 (2016).
34. M. Zhang, K. Guan, Y. Ji, G. Liu, W. Jin, N. Xu, Controllable ion transport by surface-charged graphene oxide membrane. *Nat. Commun.* **10**, 1253 (2019).
35. M. Mulder, *Basic Principles of Membrane Technology* (Kluwer Academic Publishers, Springer Science & Business Media, 1996).
36. T. Gao, L. Huang, C. Li, G. Xu, G. Shi, Graphene membranes with tuneable nanochannels by intercalating self-assembled porphyrin molecules for organic solvent nanofiltration. *Carbon* **124**, 263–270 (2017).
37. H. Yang, N. Wang, L. Wang, H.-X. Liu, Q.-F. An, S. Ji, Vacuum-assisted assembly of ZIF-8@GO composite membranes on ceramic tube with enhanced organic solvent nanofiltration performance. *J. Membr. Sci.* **545**, 158–166 (2018).
38. M. F. Jimenez-Solomon, Q. Song, K. E. Jelfs, M. Munoz-Ibanez, A. G. Livingston, Polymer nanofilms with enhanced microporosity by interfacial polymerization. *Nat. Mater.* **15**, 760–767 (2016).
39. X. Cheng, X. Jiang, Y. Zhang, C. H. Lau, Z. Xie, D. Ng, S. J. D. Smith, M. R. Hill, L. Shao, Building additional passageways in polyamide membranes with hydrostable metal organic frameworks to recycle and remove organic solutes from various solvents. *ACS Appl. Mater. Interfaces* **9**, 38877–38886 (2017).
40. M. H. Davood Abadi Farahani, T.-S. Chung, Solvent resistant hollow fiber membranes comprising P84 polyimide and amine-functionalized carbon nanotubes with potential applications in pharmaceutical, food, and petrochemical industries. *Chem. Eng. J.* **345**, 174–185 (2018).
41. C. Chen, J. Wang, D. Liu, C. Yang, Y. Liu, R. S. Ruoff, W. Lei, Functionalized boron nitride membranes with ultrafast solvent transport performance for molecular separation. *Nat. Commun.* **9**, 1902 (2018).
42. S. Xia, M. Ni, T. Zhu, Y. Zhao, N. Li, Ultrathin graphene oxide nanosheet membranes with various *d*-spacing assembled using the pressure-assisted filtration method for removing natural organic matter. *Desalination* **371**, 78–87 (2015).

43. S. Kano, H. Nakano, M. Kojima, N. Baba, K. Nakajima, An effect of the ionic radii of lanthanide(III) ions on the structure and catalytic properties of chiral Schiff base-lanthanide(III) complexes. *Inorg. Chim. Acta* **349**, 6–16 (2003).
44. X. Sui, H. Ding, Z. Yuan, C. F. Leong, K. Goh, W. Li, N. Yang, D. M. D'Alessandro, Y. Chen, The roles of metal-organic frameworks in modulating water permeability of graphene oxide-based carbon membranes. *Carbon* **148**, 277–289 (2019).
45. W.-S. Hung, C.-H. Tsou, M. De Guzman, Q.-F. An, Y.-L. Liu, Y.-M. Zhang, C.-C. Hu, K.-R. Lee, J.-Y. Lai, Cross-linking with diamine monomers to prepare composite graphene oxide-framework membranes with varying *d*-spacing. *Chem. Mater.* **26**, 2983–2990 (2014).
46. A. Klechikov, J. Yu, D. Thomas, T. Sharifi, A. V. Talyzin, Structure of graphene oxide membranes in solvents and solutions. *Nanoscale* **7**, 15374–15384 (2015).
47. C.-N. Yeh, K. Raidongia, J. Shao, Q.-H. Yang, J. Huang, On the origin of the stability of graphene oxide membranes in water. *Nat. Chem.* **7**, 166–170 (2015).
48. G. Chen, B. Han, S. Deng, Y. Wang, Y. Wang, Lanthanum dioxide carbonate $La_2O_2CO_3$ nanorods as a sensing material for chemoresistive CO_2 gas sensor. *Electrochim. Acta* **127**, 355–361 (2014).
49. Thermo Scientific, XPS Simplified: Lanthanum, https://xpssimplified.com/elements/lanthanum.php; [retrieved 11 April 2019].
50. A. He, F. Zhou, F. Ye, Y. Zhang, X. He, X. Zhang, R. Guo, X. Zhao, Y. Sun, M. Huang, Q. Li, Z. Yang, Y. Xu, J. Wu, Preparation and characterization of lanthanum carbonate octahydrate for the treatment of hyperphosphatemia. *J. Spectrosc.* **2013**, 593636 (2013).
51. X.-h. Zhang, C. He, L. Wang, Z.-q. Li, Q. Feng, Synthesis, characterization and nonisothermal decomposition kinetics of $La_2(CO_3)_3{\cdot}3.4H_2O$. *J. Therm. Anal. Calorim.* **119**, 1713–1722 (2015).
52. S. Pei, Q. Wei, K. Huang, H.-M. Cheng, W. Ren, Green synthesis of graphene oxide by seconds timescale water electrolytic oxidation. *Nat. Commun.* **9**, 145 (2018).
53. H. Schlichting, K. Gersten, *Boundary-Layer Theory* (Springer-Verlag Berlin Heidelberg, ed. 9, 2017), pp. XXVIII, 805.
54. G. Kresse, J. Furthmüller, Efficient iterative schemes for ab initio total-energy calculations using a plane-wave basis set. *Phys. Rev. B* **54**, 11169–11186 (1996).
55. J. P. Perdew, K. Burke, M. Ernzerhof, Generalized gradient approximation made simple. *Phys. Rev. Lett.* **77**, 3865–3868 (1996).
56. G. Kresse, D. Joubert, From ultrasoft pseudopotentials to the projector augmented-wave method. *Phys. Rev. B* **59**, 1758–1775 (1999).
57. S. Grimme, S. Ehrlich, L. Goerigk, Effect of the damping function in dispersion corrected density functional theory. *J. Comput. Chem.* **32**, 1456–1465 (2011).
58. G. J. Martyna, M. L. Klein, M. Tuckerman, Nosé–Hoover chains: The canonical ensemble via continuous dynamics. *J. Chem. Phys.* **97**, 2635–2643 (1992).
59. A. Lerf, H. He, M. Forster, J. Klinowski, Structure of graphite oxide revisited. *J. Phys. Chem. B* **102**, 4477–4482 (1998).
60. K. Momma, F. Izumi, *VESTA 3* for three-dimensional visualization of crystal, volumetric and morphology data. *J. Appl. Cryst.* **44**, 1272–1276 (2011).
61. B. M. Yoo, H. J. Shin, H. W. Yoon, H. B. Park, Graphene and graphene oxide and their uses in barrier polymers. *J. Appl. Polym. Sci.* **131**, 39628 (2014).
62. L. E. Nielsen, Models for the permeability of filled polymer systems. *J. Macromol. Sci. A* **1**, 929–942 (1967).
63. M. A. Priolo, K. M. Holder, T. Guin, J. C. Grunlan, Recent advances in gas barrier thin films via layer-by-layer assembly of polymers and platelets. *Macromol. Rapid Commun.* **36**, 866–879 (2015).
64. S. Wang, D. Mahalingam, B. Sutisna, S. P. Nunes, 2D-dual-spacing channel membranes for high performance organic solvent nanofiltration. *J. Mater. Chem. A* **7**, 11673–11682 (2019).
65. B. E. Poling, J. M. Prausnitz, J. P. O'Connell, *Properties of Gases and Liquids* (McGraw Hill Professional, London, 2000).
66. H. Wu, Q. Gong, D. H. Olson, J. Li, Commensurate adsorption of hydrocarbons and alcohols in microporous metal organic frameworks. *Chem. Rev.* **112**, 836–868 (2012).
67. A. Buekenhoudt, F. Bisignano, G. De Luca, P. Vandezande, M. Wouters, K. Verhulst, Unravelling the solvent flux behaviour of ceramic nanofiltration and ultrafiltration membranes. *J. Membr. Sci.* **439**, 36–47 (2013).
68. C. M. Hansen, *Hansen Solubility Parameters: A User's Handbook* (CRC Press, 2007).
69. D. Konios, M. M. Stylianakis, E. Stratakis, E. Kymakis, Dispersion behaviour of graphene oxide and reduced graphene oxide. *J. Colloid Interface Sci.* **430**, 108–112 (2014).
70. W. Zeng, Y. Du, Y. Xue, H. L. Frisch, *Physical Properties of Polymers Handbook* (Springer New York, 2007).

Acknowledgments: T.-H.B. would like to thank KAIST for the financial support. K.Z. and Y.W. acknowledge financial support from the Nanyang Environment and Water Research Institute (Core Fund), Nanyang Technological University, Singapore. **Funding:** This work was funded by GSK-EDB Trust Fund (PI: T.-H.B.). **Author contributions:** L.N. conceived and designed the experiments. J.L. and L.N. carried out the materials synthesis. L.N., Y.H., K.G., and H.E.K. performed membrane characterization. Y.W. and K.Z. performed the molecular dynamics simulation studies. L.N., K.G., M.D.G., and T.-H.B. analyzed the data and co-wrote the paper. All authors discussed the results and commented on the manuscript. **Competing interests:** The authors declare that they have no competing interests. **Data and materials availability:** All data needed to evaluate the conclusions in this paper are present in the paper and/or the Supplementary Materials. Additional data related to this paper may be requested from the authors.

Submitted 19 October 2019
Accepted 27 January 2020
Published 24 April 2020
10.1126/sciadv.aaz9184

Citation: L. Nie, K. Goh, Y. Wang, J. Lee, Y. Huang, H. E. Karahan, K. Zhou, M. D. Guiver, T.-H. Bae, Realizing small-flake graphene oxide membranes for ultrafast size-dependent organic solvent nanofiltration. *Sci. Adv.* **6**, eaaz9184 (2020).